Electric field induced injection and shift currents in zigzag graphene nanoribbons

Yadong Wei [1,2] Weiqi Li,[1] Yongyuan Jiang [1,3,4,5] and Jinluo Cheng[2,6,*]

[1]*School of Physics, Harbin Institute of Technology, 92 Xidazhi Street, Nangang, Harbin, China*
[2]*Changchun Institute of Optics, Fine Mechanics and Physics, Chinese Academy of Sciences, Changchun 130033, People's Republic of China*
[3]*Key Lab of Micro-Optics and Photonic Technology of Heilongjiang Province, Harbin, China*
[4]*Key Laboratory of Micro-Nano Optoelectronic Information System, Ministry of Industry and Information Technology, Harbin, China*
[5]*Collaborative Innovation Center of Extreme Optics, Taiyuan 030006, Shanxi, China*
[6]*School of Physical Sciences, University of Chinese Academy of Sciences, Beijing 100049, People's Republic of China*

We theoretically investigate the one-color injection currents and shift currents in zigzag graphene nanoribbons by applying a static electric field across the ribbon, which breaks the inversion symmetry to generate nonzero second-order optical responses by dipole interaction. These two types of currents can be separately excited by specific light polarization, circularly polarized lights for injection currents and linearly polarized lights for shift currents. Based on a tight binding model formed by carbon $2p_z$ orbitals, we numerically calculate the spectra of injection coefficients and shift conductivities, as well as their dependence on the static field strength and ribbon width. The spectra show many peaks associated with the optical transition between different subbands, and the positions and amplitudes of these peaks can be effectively controlled by the static electric field. By constructing a simple two band model, the static electric fields are found to modify the edge states in a nonperturbative way, and their associated optical transitions dominate the current generation at low photon energies. For typical parameters, such as a static field 10^6 V/m and light intensity 0.1 GW/cm^2, the magnitude of the injection and shift currents for a ribbon with width of 5 nm can be as large as the order of 1 μA. Our results provide a physical basis for realizing passive optoelectronic devices based on graphene nanoribbons.

I. INTRODUCTION

Graphene nanoribbon (GNR) is a narrow stripe of monolayer graphene with width varying from a few nanometers to less than 50 nanometers, at which it shows exciting physical properties in addition to graphene due to the quantum confinement [1]. Combining its compatibility with industry-standard lithographic processing [2,3] and the increasingly mature fabrication procedure [4], GNR is considered as a potential material for applications in nanoelectronics and optoelectronics. Many efforts have been devoted to understanding its band structures, transport properties, magnetism, chirality, optical properties, and so on [5–8].

The widely studied GNRs include armchair GNRs (aGNRs) with edges orientated along the armchair directions and zigzag GNRs (zGNRs) with edges orientated along the zigzag directions. The band structures of GNRs have been calculated by different models, such as first-principle calculations [1], a continuum model based on a $\boldsymbol{k} \cdot \boldsymbol{p}$ Hamiltonian [9], and a tight-binding model [10]. The simplest tight-binding model shows that zGNR is always metallic with flat bands induced by edge states, and aGNR can be either semiconducting or metallic depending on its width [10]. After considering the Coulomb interaction, density functional theory (DFT) calculations show that all narrow GNRs have finite gaps, and

zGNRs possess antiferromagnetic ground states [11]. The band gap has a strong dependence on the edge orientation and ribbon width. In such a tight-binding model, both the eigenstates and selection rules of the optical transition can be analytically obtained, and many absorption peaks are induced by the optical transitions between different subbands [12,13]. The linear optical response shows strong anisotropy along zigzag and armchair directions. With applying an external static electric field across the ribbon, the gap can be effectively tuned and becomes closed at an appropriate field strength; furthermore the optical properties are effectively modulated [14,15]. Because of the insufficient Coulomb screening, the excitonic effects are important for narrow ribbons [16–19].

In addition to linear optical responses, the nonlinear optical properties of GNR also attracted much attention. By tuning the doping level electrically, Cox *et al.* studied the plasmon-assisted harmonic generation, sum and difference frequency generation, and four-wave mixing of graphene nanostructures [20,21], and these calculated responses can be several orders of magnitude larger than that of metal nanoparticles with similar sizes. Karimi *et al.* [22] investigated the Kerr nonlinearity and third harmonic generation of GNR modulated by scatterings. Attaccalite *et al.* [23] showed the importance of excitonic effects in the third harmonic generation. Wang and Andersen studied the third harmonic generation of aGNR in the Terahertz frequencies [24–26]. Salazar *et al.* [27] studied two color coherent control of zGNR, and found that the edge states play an important role for low photon energies. Recently, Wu
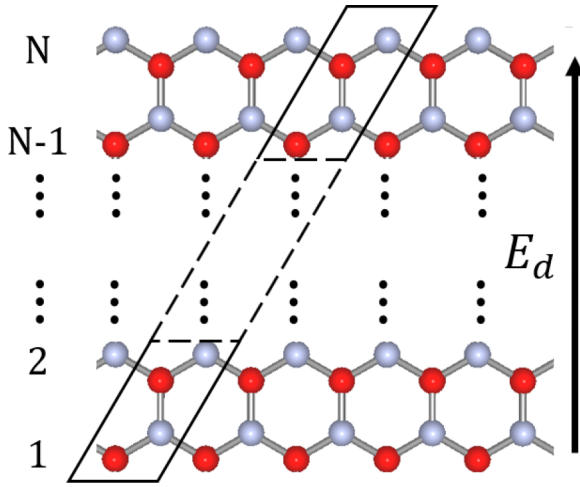
*jlcheng@ciomp.ac.cn

FIG. 1. Illustration of an N-zGNR. Red and gray dots correspond to carbon atoms at the A and B sites, respectively. The unit cell of the ribbon is indicated by the parallelogram. An external static electric field E_d is applied across the ribbon.

et al. indicated the importance of the edge states in high-order harmonic generation of zGNR [28]. Bonabi and Pedersen [29] studied the electric field induced second harmonic generation of aGNR.

In this paper, we theoretically study the one-color optical injection current and shift current of zGNR, which are direct currents generated by light with only one single frequency; they are also widely referred to as circularly photogalvanic effects and linear photogalvanic effects. These effects are recently well studied in layered materials including BiFeO$_3$ [30] and monolayer Ge and Sn monochalcogenides [31]. Because zGNR possesses the inversion symmetry, its second-order optical responses are forbidden in the dipole approximation. An external static electric field, which will be referred to as a gate field afterwards, is applied to break the inversion symmetry. We discuss the dependence of the response coefficients on the gate-field strength and the ribbon width. Our results could be useful for the optoelectronic devices utilizing the photogalvanic effects of GNR.

We arrange the paper as follows. In Sec. II we introduce a tight-binding model of zGNR with applying a static electric field, and give the expressions for injection coefficients and shift conductivities. In Sec. III we discuss the contributions from the edge bands by a simple nonperturbative treatment. In Sec. IV we discuss the effect of the ribbon width on these coefficients. We conclude in Sec. V.

II. MODELS

A. Tight-binding model for electronic states

A zGNR with N zigzag lines (N-zGNR) is illustrated in Fig. 1. Taking the x axis along the zigzag direction and the y axis along the perpendicular armchair direction with origin in the center of the ribbon, the carbon atoms locate at $\boldsymbol{R}_{nm\alpha} = n\boldsymbol{a}_1 + (m-1)\boldsymbol{a}_2 + \boldsymbol{\tau}_\alpha - \hat{\boldsymbol{y}}W/2$, where $\boldsymbol{a}_1 = a_0\hat{\boldsymbol{x}}$ is the primitive lattice vector with the lattice constant $a_0 = 2.46$ Å, $\boldsymbol{a}_2 = a_0(\hat{\boldsymbol{x}} + \sqrt{3}\hat{\boldsymbol{y}})/2$ and $m = 1, 2, \ldots, N$ labelling zigzag lines, and $\boldsymbol{\tau}_\alpha$ with $\alpha = A, B$ gives different atom sites as

$\boldsymbol{\tau}_A = 0$ and $\boldsymbol{\tau}_B = (\boldsymbol{a}_1 + \boldsymbol{a}_2)/3$. The width of a N-zGNR is $W = (N - 2/3)\sqrt{3}a_0/2$ by taking as the distance between the outermost A and B atom lines. We describe the electronic states in a tight-binding model formed by carbon $2p_z$ orbitals by considering the nearest-neighbor coupling only. When a gate field E_d is applied along the y direction, it leads to an electrostatic potential $-E_d y$, then the unperturbed Hamiltonian can be written as

$$\hat{H}_0 = \hat{H}_h - eE_d\hat{y}, \tag{1}$$

with the electron charge $e = -|e|$. The first term $\hat{H}_h$ is a hopping term with matrix elements

$$\begin{aligned}_t\langle n_1m_1A|\hat{H}_h|n_2m_2B\rangle_t &= {}_t\langle n_1m_1A|\hat{H}_h|n_2m_2B\rangle_t^* \\ &= -\gamma_0(\delta_{n_1,n_2}\delta_{m_1,m_2} + \delta_{n_1,n_2}\delta_{m_1,m_2+1} \\ &\quad + \delta_{n_1+1,n_2}\delta_{m_1,m_2}), \end{aligned} \tag{2}$$

$$_t\langle n_1m_1\alpha|\hat{H}_h|n_2m_2\alpha\rangle_t = 0, \tag{3}$$

where $\gamma_0 = 2.7$ eV is a hopping parameter between nearest neighbors [32,33], and it is consistent with recent DFT calculations [34]. The ket $|nm\alpha\rangle_t$ stands for the electronic state of the $2p_z$ orbital of the carbon atom located at $\boldsymbol{R}_{nm\alpha}$, where the orbitals in real space can be written in the form $\langle \boldsymbol{r}|nm\alpha\rangle_t = \phi(\boldsymbol{r} - \boldsymbol{R}_{nm\alpha})$. The second term is the electrostatic potential, $\hat{y}$ is the y component of the position operator $\hat{\boldsymbol{r}}$. In this model, the in-plane position operator has nonzero matrix elements only at the same site as

$$_t\langle n_1m_1\alpha_1|\hat{\boldsymbol{r}}|n_2m_2\alpha_2\rangle_t = \boldsymbol{R}_{n_1m_1\alpha_1}\delta_{n_1n_2}\delta_{m_1m_2}\delta_{\alpha_1\alpha_2}. \tag{4}$$

Here the field E_d should be treated as the total field that the electrons experience. Due to the dielectric screening, this field strength is different from the external applied dc field strength. For a wide ribbon, the total field is mostly uniform across the ribbon, and differs with the external applied static field by a factor. The dielectric screening can be treated with the inclusion of carrier-carrier interaction, which is beyond the focus of this work.

The basis Bloch states can be constructed as periodic Bloch states or the canonical Bloch states [35]. A different choice of the basis Bloch states does not affect the *band eigenstates*. In a periodic Bloch states basis formed by

$$|m\alpha, k\rangle_b = \sqrt{\frac{a_0}{2\pi}}\sum_n e^{ina_0k}|nm\alpha\rangle_t, \text{ for } 0 \leqslant k < g, \tag{5}$$

with $g = 2\pi/a_0$ being the width of the Brillouin zone, the matrix elements of the Hamiltonian $\hat{H}_0$, position operator $\hat{\boldsymbol{r}}$, and velocity operator $\hat{\boldsymbol{v}} = [\hat{\boldsymbol{r}}, \hat{H}_0]/(i\hbar)$ become

$$_b\langle m_1\alpha_1, k_1|\hat{H}_0|m_2\alpha_2, k_2\rangle_b = \tilde{H}^0_{m_1\alpha_1, m_2\alpha_2;k}\delta(k_1 - k_2), \tag{6}$$

$$\begin{aligned}_b\langle m_1\alpha_1, k_1|\hat{\boldsymbol{r}}|m_2\alpha_2, k_2\rangle_b &= \left[\tilde{\boldsymbol{r}}_{m_1\alpha_1, m_2\alpha_2;k_1} + i\hat{\boldsymbol{x}}\delta_{m_1,m_2}\delta_{\alpha_1,\alpha_2}\frac{\partial}{\partial k_1}\right] \\ &\quad \times \delta(k_1 - k_2),\end{aligned} \tag{7}$$

$$_b\langle m_1\alpha_1, k_1|\hat{\boldsymbol{v}}|m_2\alpha_2, k_2\rangle_b = \tilde{\boldsymbol{v}}_{m_1\alpha_1, m_2\alpha_2;k}\delta(k_1 - k_2). \tag{8}$$

The quantities $\tilde{P}_{m_1\alpha_1, m_2\alpha_2;k} = \sum_n e^{ina_0k}{}_t\langle nm_1\alpha_1|\hat{P}|0m_2\alpha_2\rangle_t$ for $P = H^0$, $\boldsymbol{r}$, and $\boldsymbol{v}$ are the Fourier transform of their matrix

elements in the tight-binding orbitals, and their matrix elements are

$$\tilde{H}^0_{m_1A,m_2B;k} \equiv [\tilde{H}^0_{m_2B,m_1A;k}]^* = \gamma_0(1 + e^{ika_0})\delta_{m_1m_2} + \gamma_0\delta_{m_1+1,m_2}, \tag{9}$$

$$\tilde{H}^0_{m_1\alpha,m_2\alpha;k} = -eE_d\tilde{r}^y_{m_1\alpha,m_2\alpha;k}, \tag{10}$$

and

$$\tilde{r}_{m_1\alpha_1,m_2\alpha_2;k} = \delta_{m_1m_2}\delta_{\alpha_1\alpha_2}\mathbf{R}_{0m_1\alpha_1}, \tag{11}$$

$$\tilde{\mathbf{v}}_{m_1\alpha_1,m_2\alpha_2;k} = \frac{1}{i\hbar}[\tilde{r}_k, \tilde{H}^0_k]_{m_1\alpha_1,m_2\alpha_2} + \hat{x}\frac{1}{\hbar}\frac{\partial}{\partial k}\tilde{H}^0_{m_1\alpha_1,m_2\alpha_2;k}. \tag{12}$$

In the last equation $\tilde{r}_k$ and $\tilde{H}^0_k$ are treated as matrices with indexes $m\alpha$. The gate field modifies the on-site energy of each atom.

The band eigenstates $|sk\rangle$ with band index s can be written as

$$|sk\rangle = \sum_{m\alpha}[C_{sk}]_{m\alpha}|m\alpha, k\rangle_b, \tag{13}$$

where the coefficients C_{sk} are column eigenvectors satisfying

$$\tilde{H}^0_k C_{sk} = \varepsilon_{sk}C_{sk}, \tag{14}$$

with the corresponding eigenenergy ε_{sk}.

For the optical response, the most important quantity is the Berry connection $\boldsymbol{\xi}_{s_1s_2k}$ between band eigenstates, which is defined as $\langle s_1k_1|\hat{r}|s_2k_2\rangle = \delta(k_1 - k_2)\boldsymbol{\xi}_{s_1s_2k}$ with

$$\boldsymbol{\xi}_{s_1s_2k} = C^\dagger_{s_1k}\left(\tilde{r}_k + i\hat{x}\frac{\partial}{\partial k}\right)C_{s_2k}. \tag{15}$$

The term $\xi^y_{s_1s_2k}$ can be evaluated directly. However, due to the derivative with respect to k, the values of $\xi^x_{s_1s_2k}$ depend on the phase of the eigenvectors C_{sk} and are not easy to be evaluated directly. Usually the off-diagonal terms can be evaluated from the matrix elements of velocity operator

$$\mathbf{v}_{s_1s_2k} = C^\dagger_{s_1k}\tilde{\mathbf{v}}_k C_{s_2k}. \tag{16}$$

The usually used quantities are $\mathbf{r}_k$, which are defined as

$$r^y_{s_1s_2k} = \xi^y_{s_1s_2k}, \text{ for all } s_1, s_2, \tag{17}$$

$$r^x_{s_1s_2k} \equiv \begin{cases} \xi^x_{s_1s_2k} = \dfrac{v^x_{s_1s_2k}}{i\omega_{s_1s_2k}} & \text{for } s_1 \neq s_2, \\ 0 & \text{for } s_1 = s_2, \end{cases} \tag{18}$$

with $\hbar\omega_{s_1s_2k} = \varepsilon_{s_1k} - \varepsilon_{s_2k}$. The diagonal term of ξ^x_{ssk} appears in the terms

$$\mathcal{R}^{cx}_{s_1s_2k} = \frac{\partial}{\partial k}r^c_{s_1s_2k} - i(\xi^x_{s_1s_1k} - \xi^x_{s_2s_2k})r^c_{s_1s_2k}, \text{ for } s_1 \neq s_2, \tag{19}$$

with the c in the superscript standing for the Cartesian directions x or y. A direct calculation gives

$$\mathcal{R}^{cx}_{s_1s_2k} = -\frac{\Delta^x_{s_1s_2k}r^c_{s_1s_2k}}{\omega_{s_1s_2k}} + \frac{i[r^x_k, v^c_k]_{s_1s_2} + M^{cx}_{s_1s_2}}{i\omega_{s_1s_2k}}, \tag{20}$$

with $\Delta^b_{s_1s_2k} = v^b_{s_1s_1k} - v^b_{s_2s_2k}$ and

$$M^{cx}_{s_1s_2} = C^\dagger_{s_1k}\left(\frac{\partial}{\partial k}\tilde{v}^c_k - i[\tilde{r}^x_k, \tilde{v}^c_k]\right)C_{s_2k}. \tag{21}$$

For zGNR, $\mathcal{R}^{yx}_{s_1s_2k} = i[r^x_k, r^y_k]_{s_1s_2}$.

B. Injection currents and shift currents

In this work, we are interested in the shift current and one-color injection current, both of which arise from the second-order optical response. For an incident electric field $\mathbf{E}(t) = \mathbf{E}_0(t)e^{-i\omega t} + \text{c.c.}$ with the slow varying envelope function $\mathbf{E}_0(t)$, the response current includes a (quasi) dc current component $\mathbf{J}_0(t) = J_0(t)\hat{x}$, which is along the ribbon extension direction only because a dc current cannot flow along the confined dimension. This current approximately includes two parts $J_0(t) = J_i(t) + J_s(t)$. The first term $J_i(t)$ is a one-color injection current, and it is

$$\frac{d}{dt}J_i(t) = 2i\eta^{xbc}(\omega)E^b_0(t)[E^c_0(t)]^*, \tag{22}$$

and the effective sheet injection rate is $\eta^{xbc}(\omega) = \sum_{s_1s_2}\eta^{xbc}_{s_1s_2}(\omega)$ with

$$\eta^{xbc}_{s_1s_2}(\omega) = -\frac{i\pi e^3}{W\hbar^2}\int\frac{dk}{2\pi}\Delta^x_{s_1s_2k}(r^c_{s_2s_1k}r^b_{s_1s_2k} - r^b_{s_2s_1k}r^c_{s_1s_2k})$$
$$\times f_{s_2s_1k}\delta(\omega_{s_2s_1k} - \omega). \tag{23}$$

Here $f_{s_2s_1k} = f_{s_2k} - f_{s_1k}$ gives the population difference in two states $|s_2k\rangle$ and $|s_1k\rangle$, and $f_{sk} = [1 - e^{(\varepsilon_{sk}-\mu)/k_BT}]^{-1}$ is Fermi-Dirac distribution for chemical potential μ and temperature T. The spin degeneracy was included in Eq. (23). The second term $J_s(t)$ is a shift current, and it is

$$J_s(t) = 2\sigma^{xbc}(\omega)E^b_0(t)[E^c_0(t)]^*, \tag{24}$$

where the effective sheet shift conductivity is $\sigma^{xbc}(\omega) = \sum_{s_1s_2}\sigma^{xbc}_{s_1s_2}(\omega)$ with

$$\sigma^{xbc}_{s_1s_2}(\omega) = -\frac{i\pi e^3}{W\hbar^2}\int\frac{dk}{2\pi}f_{s_2s_1k}(r^b_{s_1s_2k}\mathcal{R}^{cx}_{s_2s_1k} + r^c_{s_1s_2k}\mathcal{R}^{bx}_{s_2s_1k})$$
$$\times \delta(\omega_{s_2s_1k} - \omega). \tag{25}$$

Note that the expressions in Eqs. (23) and (25) are derived following the work by Sipe and Shkrebtii [36], and they are gauge independent with respect to the phases of band eigenstates.

Here we briefly discuss the general properties of $\eta^{xbc}(\omega)$ and $\sigma^{xbc}(\omega)$ from the symmetry argument. The response coefficients of $\eta^{xbc}(\omega)$ and $\sigma^{xbc}(\omega)$ are third-order tensors. As a static electric field is applied along the y direction, a zGNR possesses a symmetry $x \leftrightarrow -x$ and the time reversal symmetry. We list the results for A^{xbc} ($A \to \eta$ or σ_s) under each symmetry operation:. (1) The symmetry $x \leftrightarrow -x$ determines that the nonzero components are A^{xxy} and A^{xyx}. (2) A direct observation of Eqs. (23) and (25) gives $\eta^{xbc}(\omega) = -\eta^{xcb}(\omega)$ and $\sigma^{xbc}_s(\omega) = \sigma^{xcb}_s(\omega)$. (3) The time reversal symmetry [36] gives $\mathbf{r}_{s_1s_2k} = \mathbf{r}_{s_2s_1(-k)} = [\mathbf{r}_{s_1s_2(-k)}]^*$, $\mathbf{v}_{s_1s_2k} = -\mathbf{v}_{s_2s_1(-k)} = -[\mathbf{v}_{s_1s_2(-k)}]^*$, and $\varepsilon_{sk} = \varepsilon_{s(-k)}$. Furthermore, we can derive $\Delta^a_{s_1s_2k} = -[\Delta^a_{s_1s_2(-k)}]^*$ and $\mathcal{R}^{cx}_{s_1s_2k} = -\mathcal{R}^{cx}_{s_2s_1(-k)} = -[\mathcal{R}^{cx}_{s_1s_2(-k)}]^*$. Then we get $\eta^{xbc}(\omega) = [\eta^{xbc}(\omega)]^*$ from Eq. (23) and $\sigma^{xbc}(\omega) = [\sigma^{xbc}(\omega)]^*$ from Eq. (25). Using the operations (1) to (3) we find the nonzero components $\eta^{xxy}(\omega) = -\eta^{xyx}(\omega)$ and $\sigma^{xxy}_s(\omega) = \sigma^{xyx}_s(\omega)$ are real numbers.
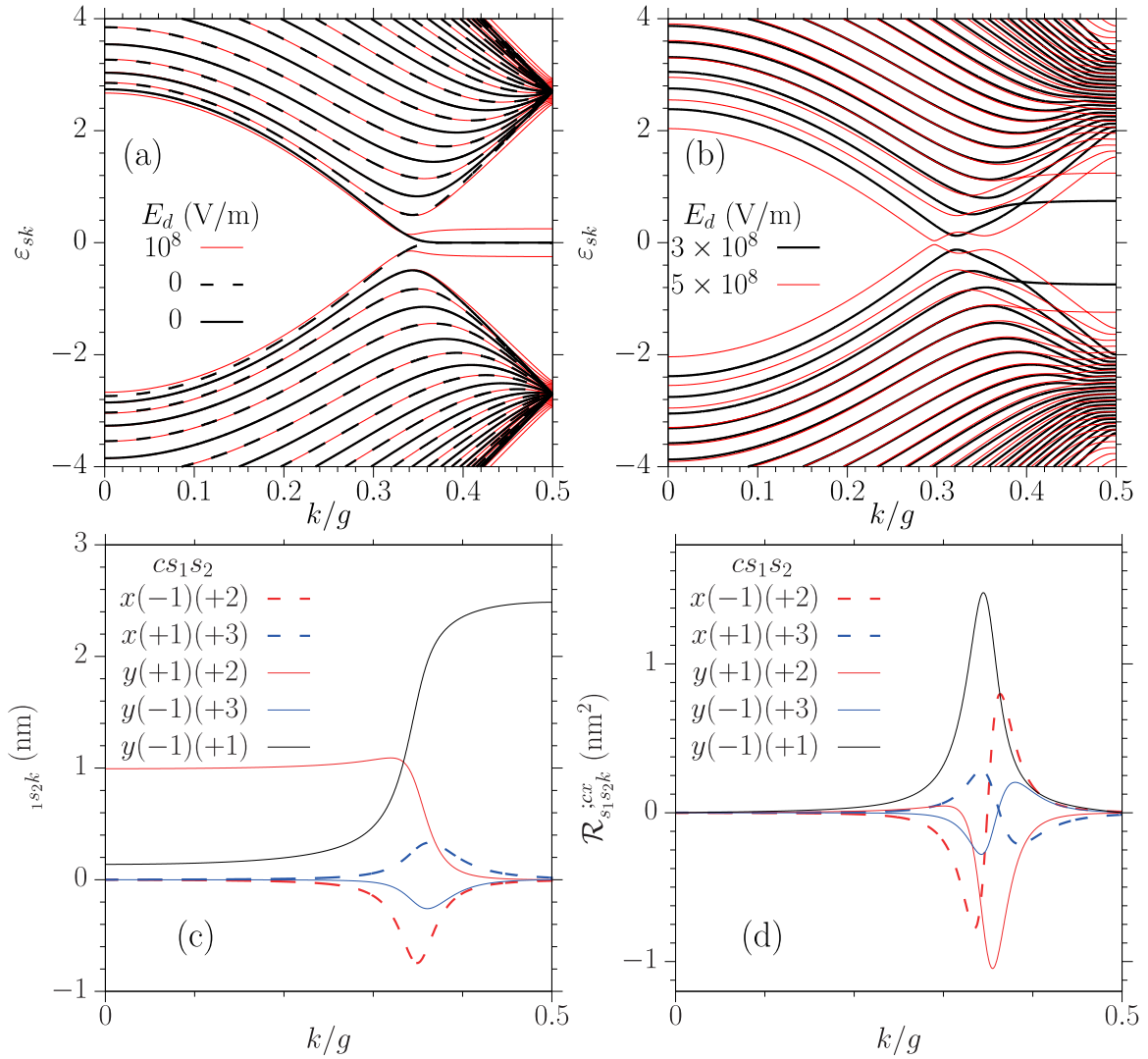
FIG. 2. (a), (b) Band structures of 24-zGNR for gate field $E_d = 0$, 10^8 V/m, 3×10^8 V/m, and 5×10^8 V/m. At zero field, the dashed and solid curves correspond to different parity. The matrix elements of (c) $r^{0;c}_{s_1 s_2 k}$ and (d) $\mathcal{R}^{0;cx}_{s_1 s_2 k}$ at zero gate field, with solid (dashed) curves for imaginary (real) parts.

More specifically, by taking the light fields as $\boldsymbol{E}_0(t) = E_0(t)\left(\begin{smallmatrix} \cos\theta \\ e^{i\phi}\sin\theta \end{smallmatrix}\right)$, the injection and shift currents can be written as

$$\frac{d}{dt}J_i(t) = 4\eta^{xxy}(\omega)[E_0(t)]^2 \cos\theta \sin\theta \sin\phi, \quad (26)$$

$$J_s(t) = 4\sigma^{xxy}(\omega)[E_0(t)]^2 \cos\theta \sin\theta \cos\phi. \quad (27)$$

Here θ and ϕ are the polarization orientation angles with respect to the direction $\hat{\boldsymbol{x}}$ and the circularity, respectively. Therefore, the appearance of these currents requires both the x and y components of the electric field. The circularly polarized light ($\phi = \pi/2$) generates injection currents only, while the linearly polarized light ($\phi = 0$) generates shift currents only.

III. RESULT AND DISCUSSIONS

A. Band structure

We illustrate the band structures of a 24-zGNR ($W \approx 5$ nm) for different gate field E_d in Figs. 2(a) and 2(b). The bands

with energies higher than zero are labeled by $s = +1, +2, \ldots$ successively from low-energy band to high-energy band, and those with energy lower than zero are labeled by $s = -1, -2, \ldots$ in a mirror way. From the symmetry $x \rightarrow -x$, the band energies satisfy $\varepsilon_{sk} = \varepsilon_{s(g-k)}$ and $\varepsilon_{sk} = -\varepsilon_{(-s)k}$, and thus they are shown only in half of the Brillouin zone. The band structure at zero gate field is plotted in Fig. 2(a) as black solid and dashed curves. The two bands $s = \pm 1$ are almost flat in the middle of the Brilluion zone, indicating the edge states. The energy difference $\varepsilon_{(+1)k} - \varepsilon_{(-1)k}$ decreases as k approaches $g/2$ and becomes less than 1 meV for $0.38g < k < 0.62g$. At $k = g/2$, the two states are strictly degenerate. All other electronic states are confined states. At $k = g/2$, all the states $|sg/2\rangle$ for $s > 1$ are degenerate at energy γ_0, and all states $|sg/2\rangle$ for $s < -1$ are degenerate at energy $-\gamma_0$. At zero gate field, the inversion symmetry is preserved, and the parity is a good quantum number for each band as $\zeta_s = (-1)^{s+1}\mathrm{sgn}[s]$ [13,27], which is shown in the dashed and solid curves in Fig. 2(a). There exist selection rules for the velocity matrix elements as $v^x_{s_1 s_2 k} = 0$ for $\zeta_{s_1} \neq \zeta_{s_2}$ and

$v^y_{s_1 s_2 k} = 0$ for $\zeta_{s_1} = \zeta_{s_2}$, and the same selection rules hold for $\boldsymbol{\xi}_{s_1 s_2 k}$. Therefore, the nonzero $\xi^y_{s_1 s_2 k}$ between bands with different parities indicates that the gate field can couple bands with different parities and then the band parity is no longer a good quantum number.

Figure 2(c) gives the k dependence of $r^{0;c}_{s_1 s_2 k}$ for different sets of $cs_1 s_2$, where a quantity at zero gate field is indicated by a superscript "0." With choosing the wave functions appropriately [37] $r^{0;x}_{s_1 s_2 k}$ can be set as pure imaginary numbers and $r^{0;y}_{s_1 s_2 k}$ as real numbers. For $r^{0;y}_{(-1)(+1)k}$, it is close to a value $W/2 = 2.5$ nm for edge states and decreases for confined states ($k < 0.34g$) as k decreases to 0. Figure 2(d) gives the k dependence of $\mathcal{R}^{0;cx}_{s_1 s_2 k}$ for the same sets of $cs_1 s_2$, which locates at around $k \sim 0.33g$. We also compared the values $\partial_k r^{0;c}_{s_1 s_2 k}$ and $\mathcal{R}^{0;cx}_{s_1 s_2 k}$, and they show negligible difference, which indicates all $\xi^{0;x}_{ssk}$ can be taken as zero, as used in the Appendix.

The band structure at a gate field $E_d = 10^8$ V/m is also plotted in Fig. 2(a). Such a gate field mostly affects the bands $s = \pm 1$. It opens the degenerate point at $k = g/2$ to an energy difference $|e|E_0 W \sim 0.5$ eV, and separates the two nearly degenerate flat bands with energies around ± 0.25 eV. The gap of these two bands is about ~ 0.3 eV located at $k \sim 0.34g$. The band structures at stronger gate field $E_d = 3 \times 10^8$ V/m and 5×10^8 V/m are shown in Fig. 2(b). In both cases, the gate fields can significantly affect more bands including $s = \pm 2$ and $s = \pm 3$. When the field strength E_d is large enough, the gap can be closed again, and all bands are significantly modified. In this work, we limit the gate field $E_d < 10^8$ V/m to ensure the reasonableness of our tight-binding model.

To better understand the effects of a weak gate field on the edge states, we present a simple two-band model. The sub-Hilbert space is formed by $\{|(+1)k\rangle^0, |(-1)k\rangle^0\}$. The Hamiltonian in this subspace is

$$H^{\text{edge}}_k = \begin{pmatrix} \epsilon_k & d_k \\ d_k & -\epsilon_k \end{pmatrix}, \tag{28}$$

where $\epsilon_k = \varepsilon^0_{(+1)k}$ is the energy of band "+1" at zero gate field, and $d_k = |e|E_d r^{0;y}_{(+1)(-1)k}$ is the coupling strength, which can be chosen as a real positive number. We used $\xi^{0;y}_{ssk} = 0$ to obtain Eq. (28). From Fig. 2(c) the matrix element of $r^{0;y}_{(+1)(-1)k}$ is around $W/2$ for the edge states $k \sim g/2$, but decreases as k moves to 0. The Hamiltonian in Eq. (28) has the eigenstates

$$|sk\rangle = \frac{1}{\sqrt{2}} [s\sqrt{1+sN_k}|(+1)k\rangle^0 + \sqrt{1-sN_k}|(-1)k\rangle^0],$$
$$\text{for } s = \pm 1, \tag{29}$$

and the eigenenergies

$$\varepsilon_{sk} = s\sqrt{\epsilon_k^2 + d_k^2}, \tag{30}$$

with $N_k = \epsilon_k/\varepsilon_{(+1)k}$. For edge states at $k = g/2$, $\epsilon_k = 0$, and $\varepsilon_{sk} = s|e|E_d W/2$; as k moves towards 0, ϵ_k increases slowly till $k < g/3$ but d_k decreases quickly, which gives a dip in the spectra of ε_{+k} around $k \sim g/3$; when k moves further, the bands $s = \pm 1$ are no longer nearly degenerate, and the effect of the gate field can be treated as a perturbation.

The effects of the gate field on higher bands are basically perturbative, thus, to focus on the influence of the edge states, we calculate the Berry connections of the electronic states $\{|sk\rangle, |lk\rangle^0; s = \pm 1, l \neq \pm 1\}$ as

$$\boldsymbol{\xi}_{slk} = \frac{1}{\sqrt{2}} [s\sqrt{1+sN_k}\boldsymbol{\xi}^0_{(+1)lk} + \sqrt{1-sN_k}\boldsymbol{\xi}^0_{(-1)lk}], \tag{31}$$

$$\boldsymbol{\xi}_{(+1)(-1)k} = \frac{1}{2} \frac{i\partial_k N_k}{\sqrt{1-N_k^2}}\hat{\boldsymbol{x}} + N_k \xi^{0;y}_{(+1)(-1)k}\hat{\boldsymbol{y}}. \tag{32}$$

A detailed derivation is given in the Appendix.

B. Injection coefficients of 24-zGNR

We turn to the numerical evaluation of the injection coefficients in Eq. (23) and the shift conductivity in Eq. (25). During the numerical evaluation, the Brillouin zone is divided into a 3100 grid, the δ function is approximated by a Gaussian function

$$\delta(\hbar\omega_{s_1 s_2 k} - \hbar\omega) \rightarrow \frac{1}{\sqrt{\pi}\Delta} e^{-(\hbar\omega_{s_1 s_2 k} - \hbar\omega)^2/\Delta^2}, \tag{33}$$

with a broadening width $\Delta = 2$ meV, and the temperature is chosen at room temperature. The functions $\delta(\hbar\omega_{ss'k} - \hbar\omega)$ are associated with the joint density of states, which gives the weight to the optical transition from the s' band to the s band. It can be evaluated exactly as

$$\delta(\hbar\omega_{ss'k} - \hbar\omega) = \sum_j \frac{1}{\hbar|\Delta_{ss'k}|}\delta(k - k_j), \tag{34}$$

with k_j satisfying $\omega_{ss'k_j} = \omega$.

In Fig. 3(a) the energy differences $\hbar\omega_{ss'k}$ are plotted with respect to k for different band pairs (s, s') with the condition that $|f_{sk} - f_{s'k}| \sim 1$. The energy differences $\hbar\omega_{s(-1)k}$ and $\hbar\omega_{s(-2)k}$ show valleys around $k \sim g/3$ for all $s > 1$, while $\hbar\omega_{s(+1)k}$ shows valleys only for bands with $s \geqslant 6$. These valleys determine the transition edge between these bands and lead to divergent joint density of states from Eq. (34). However, there is no such point for $\hbar\omega_{(+1)(-1)k}$ at zero gate field. For the nonzero gate field, $\hbar\omega_{(+1)(-1)k}$ shows a valley at around a similar k value $\sim g/3$, as discussed above. In Fig. 3(b), the gaps between these band pairs are plotted as functions of the gate field, and the color bar shows the k values of the gap. The gate field modifies the gap between the bands (± 1) significantly.

Figure 4 gives the spectra of injection coefficients of a 24-zGNR at different E_d. In general, the effects of a small E_d can be treated perturbatively and the injection coefficients can be connected with a third-order sheet response coefficients as

$$\eta^{xbc}_{s_1 s_2}(\omega) = \tilde{\eta}^{xbcy}_{s_1 s_2}(\omega)E_d. \tag{35}$$
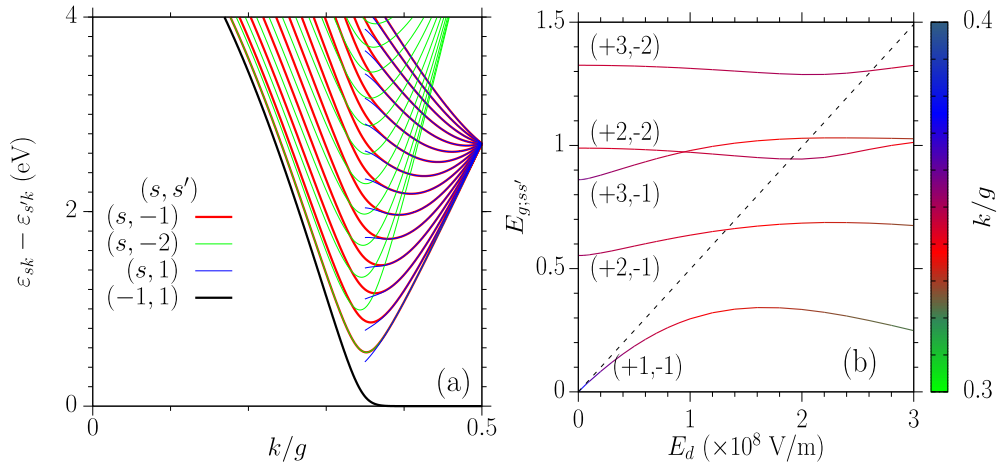
FIG. 3. (a) The energy difference $\varepsilon_{sk} - \varepsilon_{s'k}$ for different (s, s') pairs at zero gate field. (b) The gate-field dependence of the energy gaps $E_{g,ss'}$ between different bands (s, s'). The line color indicates the k values of these gaps. The black dotted line gives the energy difference $\varepsilon_{(1)g/2} - \varepsilon_{(-1)g/2}$.

Figure 4(a) plots the spectra of $\tilde{\eta}^{xbcy}(\omega)$ for $E_d = 10^2$, 10^4, 10^6, and 10^7 V/m. When the photon energy is higher than the gap, the injection occurs. As the photon energy increases, the injection coefficient increases rapidly to the first peak, and afterwards it shows more peaks and the magnitude of each peak decreases with the photon energy. The first five peaks are located at around $\hbar\omega \sim 0.04$, 0.53, 0.85, 1.16, and 1.45 eV; they slightly depend on the broadening parameter Δ because the Dirac function is approximated by a Gaussian function. When the photon energy is higher than 2.5 eV, the injection coefficients are about zero. As the field E_d increases from 10^2 V/m to 10^7 V/m, the value of $\tilde{\eta}^{xbxy}(\omega)$ changes little for the photon energies in certain windows ($\hbar\omega \in [0.2, 0.4]$ eV and a small energy range around 0.5 eV). Such an energy window is enlarged to [0.1,0.6] eV if the gate field E_d is between 10^2 V/m and 10^6 V/m. The existence of these windows identifies the photon energies that the perturbative treatment in Eq. (35) is appropriate. However, for photon energies $\hbar\omega > 1$ eV, although the injection coefficients are small, they differ significantly even for $E_d = 10^2$ V/m and 10^4 V/m, indicating a nonperturbative feature of zGNR under electric fields.

The peaks are mostly induced by the optical transitions associated with the edge bands $s = \pm 1$, as shown in Fig. 4(b), where the spectra of $\tilde{\eta}_{(+1)(-1)}^{xxyy}(\omega)$ and $\tilde{\eta}_l = \tilde{\eta}_{l(+1)}^{xxyy} + \tilde{\eta}_{l(-1)}^{xxyy} + \tilde{\eta}_{(+1)(-l)}^{xxyy} + \tilde{\eta}_{(+1)(-l)}^{xxyy}$ are plotted for $E_d = 10^4$ V/m. The electron-hole symmetry ensures $\tilde{\eta}_{s_1 s_2}^{xxyy} = \tilde{\eta}_{-s_2-s_1}^{xxyy}$ for an undoped ribbon. To better understand these nonperturbative features, from Eq. (23), we write the injection coefficient as

$$\tilde{\eta}_{s_1 s_2}^{xxyy}(\omega) = \frac{e^3}{E_d W \hbar^2} \sum_j \mathrm{sgn}(\Delta_{s_1 s_2 k_j}^x) \mathrm{Im}\big[r_{s_2 s_1 k_j}^y r_{s_1 s_2 k_j}^x\big] f_{s_2 s_1 k_j},$$

(36)

where k_j are solutions of $\omega_{s_1 s_2 k_j} - \omega = 0$ and $\mathrm{sgn}(x)$ is a sign function. Equation (36) shows that the joint density of states are canceled out with the carrier velocity. For the contribution from the transitions between the sth edge band and other bands $l \neq \pm 1$, the coefficients can be obtained using the re-

sults in the Appendix as

$$\tilde{\eta}_{ls}^{xxyy}(\omega) = \frac{e^3}{E_d W \hbar^2} \frac{s}{2} \sum_j \sqrt{1 - N_{k_j}^2} \mathrm{Im}\big[\xi_{s'lk_j}^{0;x} \xi_{(-s')lk_j}^{0;y}\big](-f_{sk_j}).$$

(37)

As an example, the spectra of $\tilde{\eta}_{(+3)(+1)}$ and $\tilde{\eta}_{(+3)(-1)}$ are shown in Fig. 4(b). Their values are nearly opposite, thus their sum is much smaller, which indicates an interesting cancellation between the transitions. Because of the nearly degenerate edge bands, the dependence on E_d of the injection coefficients is complicated.

For higher gate fields, the band structures are dramatically changed, and the understanding of the current injection cannot be based on the quantities of ungated ribbons. The contribution from $\tilde{\eta}_{s(+1)}$ becomes negligible because there is less occupation on the band $s = 1$. Figures 4(c) and 4(d) give the spectra of $\eta^{xyy}(\omega)$ at $E_d = 10^7$, 5×10^7, and 10^8 V/m. For low photon energy, the injection occurs between the bands $s = -1$ and $s = 1$. As the electric field increases from 10^7 to 10^8 V/m, the injection coefficients remain almost unchanged, instead, the peak position changes significantly, indicating the changes of the band structure. Similar to the cases at small gate fields, the injection coefficients decrease with the photon energy quickly.

We give an estimation on how large the injection current can be at a gate field 10^6 V/m. The injection current usually depends on both the carrier relaxation time and laser pulse duration Δ [38]. Considering that the carrier relaxation time strongly depends on the sample quantity and its surrounding environment, the injection current is estimated just from laser pulse duration as $J \sim \frac{dJ}{dt} \Delta = 2\tilde{\eta}^{xxyy} E_d |E_0|^2 \Delta$. At the photon energy 0.55 eV around the second peak, our calculated current injection rate is about 0.1 $m^2 V^{-2} s^{-1}$, it corresponds to the bulk current injection rate $\sim 2 \times 10^{10} \mu A s^{-1} V^{-2}$ considering the 0.3-nm thickness of zGNR, which is nearly 25 times larger than that in bulk GaAs [39]. In this case, a laser pulse with intensity 0.1 GW/cm^2 and duration 1 ps can generate an injection current $\sim 1.1 \mu A$.

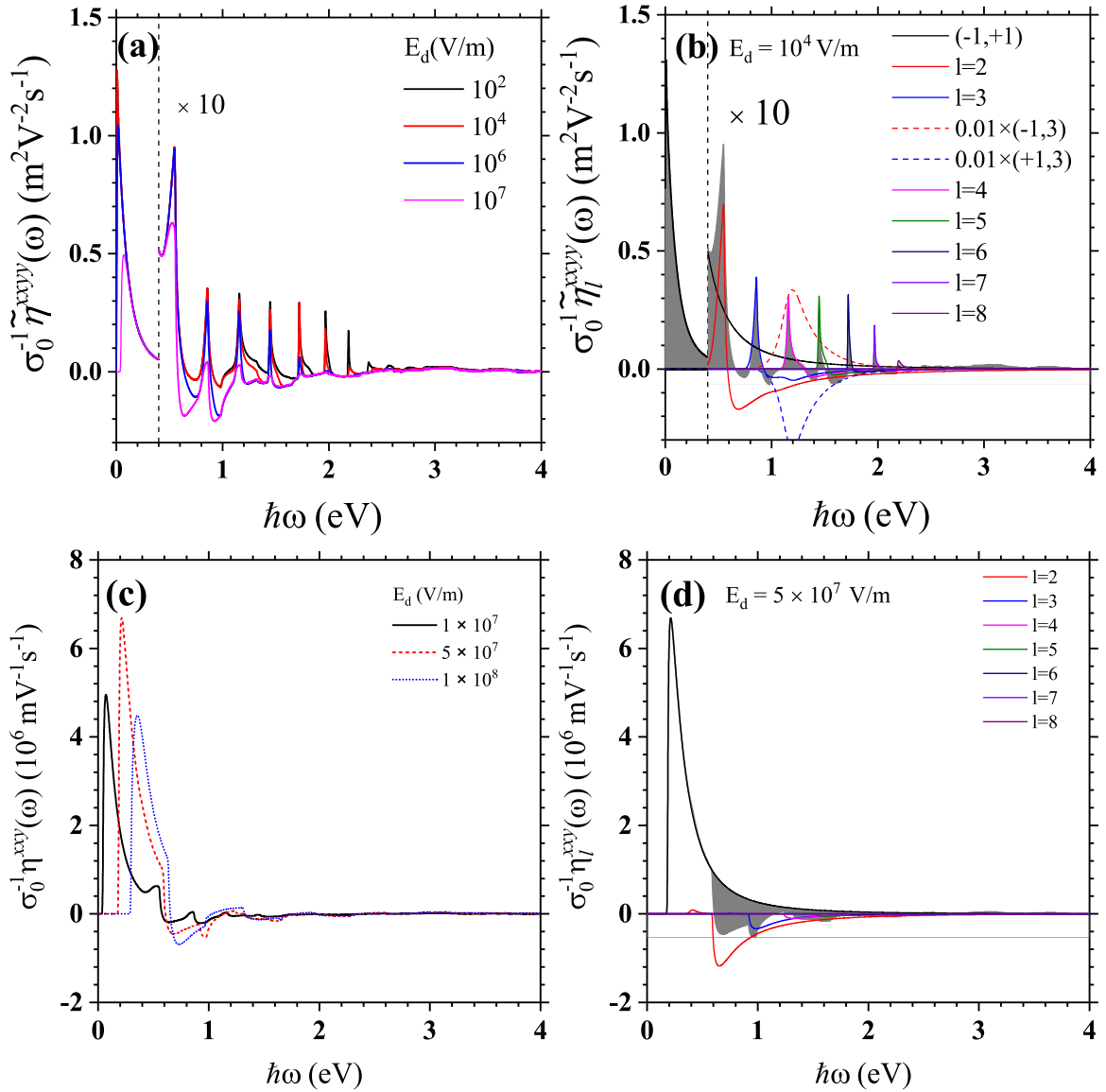FIG. 4. (a) Spectra of injection coefficient $\tilde{\eta}^{xxyy}(\omega)$ for a 24-zGNR for gates fields $E_d = 10^2$, 10^4, 10^6, and 10^7 V/m at room temperature; the curves at the right of the vertical dashed line are scaled by ten times. (b) The spectra of $\tilde{\eta}^{xxyy}_{(+1)(-1)}$ and $\tilde{\eta}^{xxyy}_l$ for $l = 2, 3, \ldots, 8$ for $E_d = 10^2$ V/m. Two specific labels mark the separated contribution of transition from band ± 1 to the band $l = 3$. (c) The injection coefficient η^{xxy} of zGNR under large electric field $E_d = 10^7$, 5×10^7, and 10^8 V/m at room temperature. (d) The spectra of $\tilde{\eta}^{xxy}_l$ for $l = 2, 3, \ldots, 8$ for $E_d = 5 \times 10^7$ V/m.

C. Shift conductivity of 24-zGNR

Figure 5(a) gives spectra of $\sigma^{xxy}(\omega)$ as well as the contributions from different optical transitions for a gate field $E_d = 10^4$ V/m. The spectra show the following features. (1) The values of the shift conductivity decrease quickly with the photon energy for $\hbar\omega < 0.5$ eV, and drop suddenly at $\hbar\omega \sim 0.55$ eV to a very sharp valley, which is induced by the divergent joint density of states between the bands ± 1 and ± 2. (2) With increasing the photon energy, the conductivity shows positive peaks and negative valleys alternatively. The first four valleys are located at 0.97, 1.33, 1.74, and 2.19 eV, and the first four peaks are located at 1.15, 1.53, 1.97, and 2.41 eV; other peaks and valleys have much smaller ampli-

tudes. (3) The peaks and valleys have different widths, and the widths for the third peak and the fourth valley are very narrow. These peaks and valleys can be better understood from transition-resolved conductivities, which are also plotted in Fig. 5(a) for $\sigma^{xxy}_{(+1)(-1)}(\omega)$, $\sigma^{xxy}_{(+3)(\pm 1)}(\omega)$, as well as $\sigma^{xxy}_l(\omega) = \sum_{\pm} \sigma^{xxy}_{(+l)(\pm 1)}(\omega) + \sigma^{xxy}_{(\pm 1)(-l)}(\omega)$ for $l = 2, 3, 4, 5$. Similar to the injection processes, $\sigma^{xxy}_{(+s)(+s')}(\omega) = \sigma^{xxy}_{(-s')(-s)}(\omega)$ holds for an undoped ribbon. However, different from the injection process, the values of $\sigma^{xxy}_{(+s)(\pm 1)}$ and $\sigma^{xxy}_{(\pm 1)(-s)}$ have similar amplitudes and the same signs but are located at different photon energies, and their total contribution leads to a wider peak or valley compared to those in the injection coefficients shown in Fig. 4(b). The transition σ^{xxy}_2 is composed of two valleys: one
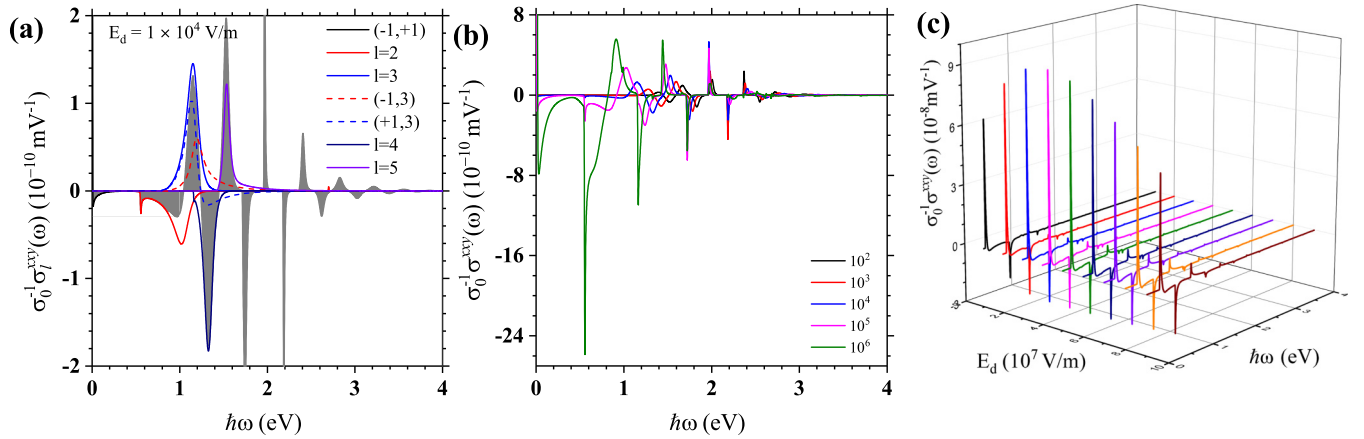
FIG. 5. Spectra of shift conductivity $\sigma^{xxy}(\omega)$ for an undoped 24-zGNR at different gate fields. (a) Transition-resolved contribution of $\sigma^{xxy}(\omega)$ at $E_d = 10^4$ V/m. The shadowed region gives the total conductivity. The plotted contribution from different band pairs are $\sigma^{xxy}_{(+1)(-1)}(\omega)$, $\sigma^{xxy}_{(+3)(\pm1)}(\omega)$, as well as $\sigma^{xxy}_l(\omega) = \sum_{\pm} \sigma^{xxy}_{(+l)(\pm1)}(\omega) + \sigma^{xxy}_{(\pm1)(-l)}(\omega)$ for $l = 2, 3, 4, 5$. (b) Spectra of $\sigma^{xxy}(\omega)$ at $E_d = 10^2, 10^3, 10^4, 10^5,$ and 10^6 V/m at room temperature. (c) Spectra of $\sigma^{xxy}(\omega)$ at gate fields up to 10^8 V/m.

is at lower photon energy, which is induced by the divergent joint density of states at 0.56 eV, and the other is at higher photon energy around 1 eV.

In Fig. 5(b) the shift conductivities for $E_d = 10^2, 10^3, 10^5,$ and 10^6 V/m are plotted for a comparison. Similar to the injection processes, the shift conductivities for photon energies lower than 0.6 eV are mostly contributions from the transition between two edge bands, and they are linearly proportional to the gate field. As the gate field E_d increases from 10^2 V/m to 10^6 V/m, the location of the first valley does not change because of the negligible band-gap shift, but the peak value increases linearly from 2.5×10^{-12} m^2/V^2 to 2.5×10^{-8} m^2/V^2. For photon energies higher than 0.6 eV, the near-degenerate edge states on the flat bands play an important role and the effects of gate field lie in the non-perturbative regime, and the values for the shift conductivity are almost at the same order of magnitude. In addition, the locations of peaks and valleys shift to lower photon energies as the gate field increases. Figure 5(c) gives the spectra of the shift conductivity for gate field up to 1×10^8 V/m. For large E_d, the values around the first two peaks are much larger; the first peak value shows a maximum around $E_d = 4 \times 10^7$ V/m, while the value of the second valley changes little.

As in the case of injection current, we estimate the magnitude of the shift current of zGNR for a gate field 10^6 V/m. At the photon energy 0.56 eV around one of the valleys, the sheet shift conductivity is 1.57×10^{-13} AmV^{-2}. It corresponds to the bulk photocurrent conductivity 524 μAV^{-2}, which is two times larger than that in two-dimensional (2D) GeSe (200 μAV^{-2}) [31]. A laser intensity 0.1 GW/cm^2 can generate a shift current $\sim$0.29 μA, a few times smaller than the injection currents.

IV. WIDTH DEPENDENCE

Figure 6 gives injection coefficients and shift conductivities for zGNR with different widths $W = 5, 10, 15,$ and 20 nm

(corresponding to $N = 24, 48, 72,$ and 96) at two gate fields $E_d = 10^4$ V/m and 5×10^7 V/m. With the increase of the ribbon width, there appear more subbands, and the energy difference of neighbor bands decreases. Therefore, both for the injection coefficients and for shift conductivities, there exist more peaks or valleys in the spectra with the increase of the ribbon width, while their amplitudes change little. A wider ribbon can generate larger currents.

For very narrow zGNR with a few zigzag lines, the interaction between carriers at both edges plays an important role to form antiferromagnetic order, for which the spin orientations are opposite for different edges. The antiferromagnetic ground states lead to a finite band gap [1], which can be measured by transport experiment [40,41] and are sensitive to doping [41]. With the increase of the width of zGNR, the ferromagnetic-antiferromagnetic energy differences per unit cell decreases to below the order of 1 meV for $N > 30$ ($W > 6.3$ nm) [1]. The discussion of magnetic ground states is required to include the carrier-carrier interaction, while in this paper we focus on the illustration of the effects of the gate field; thus the contribution from the magnetic ground state is neglected, even for 24-zGNR.

V. CONCLUSION

Based on a simple tight-binding model, we explored the one-color injection currents and shift currents in zigzag graphene nanoribbons, where a gate field across the ribbon is applied to break the inversion symmetry. The gate field lifts the degeneracy of the edge bands and significantly modifies their wave functions, which leads to the nonperturbative behavior with respect to even very weak gate fields. The spectra of injection coefficients and shift conductivities show fruitful structures, including many peaks and valleys, with locations strongly depending on the ribbon width. These fine structures indicate the importance of the contributions from different bands. The injection coefficients are almost positive for different photon energies, while the sign of the shift conductivities
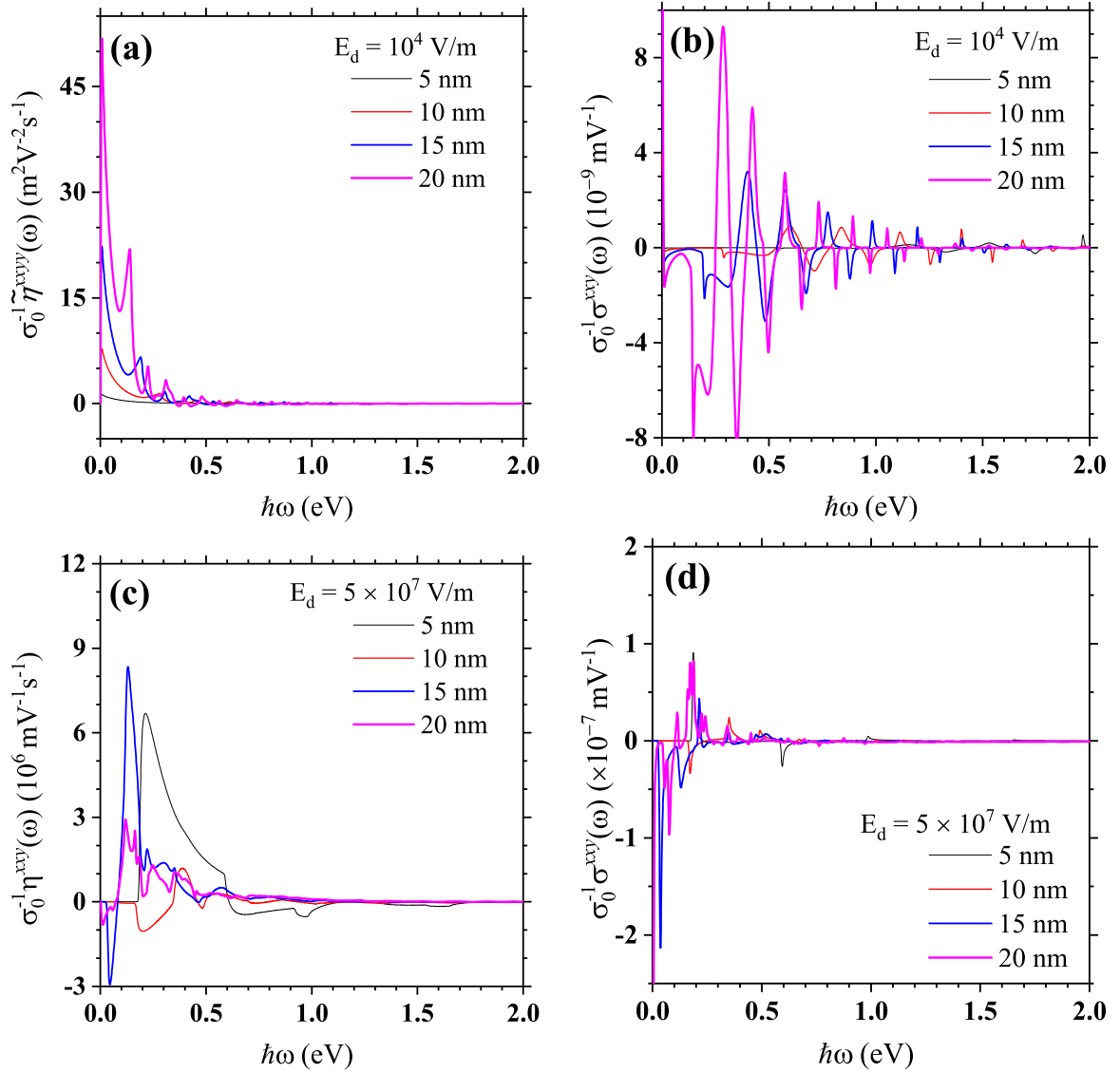
FIG. 6. The spectra of injection coefficients and shift conductivities for different ribbon width $W = 5$, 10, 15, and 20 nm. (a) $\tilde{\eta}^{xxy}(\omega)$ at $E_d = 10^4$ V/m, (b) $\sigma^{xxy}(\omega)$ at $E_d = 10^4$ V/m, (c) $\tilde{\eta}^{xxy}(\omega)$ at $E_d = 5 \times 10^7$ V/m, (d) $\sigma^{xxy}(\omega)$ at $E_d = 5 \times 10^7$ V/m.

is very sensitive on the photon energies. Under excitation by a pulsed laser with intensity 0.1 GW/cm^2, our calculation for a 5-nm-wide zGNR shows that the injection current reaches ~ 1.1 μA for a pulse with duration 1 ps, whereas the shift current is ~ 0.29 μA. Because the injection current and the shift current can be separately excited using light with different polarization and their magnitudes can be well tuned by the static electric field strength, these features could be experimentally observed.

APPENDIX: BERRY CONNECTIONS OF EDGE STATES

When there is no gate field, the wave functions can be chosen to satisfy

$$\xi^{0;x}_{(+1)(-1)k} = 0, \tag{A1}$$

$$\xi^{0;y}_{(+1)(-1)k} = \xi^{0;y}_{(-1)(+1)k} \text{ as real numbers.} \tag{A2}$$

From Fig. 2 we calculated the results of the left-hand side of

$$\mathcal{R}_{smk}^{0;cx} - \partial_k r_{smk}^{0;c} = i\big(\xi_{ssk}^{0;x} - \xi_{mmk}^{0;x}\big)r_{smk}^{0;c}, \text{ for } m = \pm 1, \pm 2, \dots, \tag{A3}$$

and found that all of them are zero in our numerical resolution. Thus in the following we will adopt $\xi_{ssk}^{0;x} - \xi_{llk}^{0;x} = 0$ without giving an exact derivation. In the new basis of $\{|sk\rangle, |lk\rangle^0\}$, the position matrix elements are

$$\langle sk|\tilde{\boldsymbol{r}}_k + i\hat{\boldsymbol{x}}\partial_k|lk\rangle^0 = \frac{1}{\sqrt{2}}\big[s\sqrt{1 + sN_k}\boldsymbol{\xi}_{(+1)lk}^0 + \sqrt{1 - sN_k}\boldsymbol{\xi}_{(-1)lk}^0\big]. \tag{A4}$$

With the inclusion of the gate field, the diagonal Berry connections can be written as

$$\xi_{ssk}^x = \langle sk|\tilde{r}_k^x + i\partial_k|sk\rangle = \frac{i}{2}\big[(1 + sN_k)\xi_{(+1)(+1)k}^{0;x} + (1 - sN_k)\xi_{(-1)(-1)k}^{0;x}\big], \tag{A5}$$

then we get

$$\xi_{(+1)(+1)k}^x - \xi_{(-1)(-1)k}^x = iN_k\big[\xi_{(+1)(+1)k}^{0;x} - \xi_{(-1)(-1)k}^{0;x}\big] = 0. \tag{A6}$$

The off-diagonal Berry connections are

$$\xi_{(+1)(-1)k}^x = \frac{i}{2}\frac{\partial_k N_k}{\sqrt{1 - N_k^2}}, \tag{A7}$$

$$\xi_{(+1)(-1)k}^y = N_k\xi_{(+1)(-1)k}^{0;y}. \tag{A8}$$

Further we can calculate

$$\mathcal{R}_{(+1)(-1)k}^{cx} = \partial_k\xi_{(+1)(-1)k}^c, \tag{A9}$$

$$\mathcal{R}_{slk}^{cx} = \partial_k\xi_{slk}^c. \tag{A10}$$

[1] Y. W. Son, M. L. Cohen, and S. G. Louie, Phys. Rev. Lett. **97**, 216803 (2006).

[2] K. A. Ritter and J. W. Lyding, Nat. Mater. **8**, 235 (2009).

[3] C. Berger, Z. Song, T. Li, X. Li, A. Y. Ogbazghi, R. Feng, Z. Dai, A. N. Marchenkov, E. H. Conrad, P. N. First, and W. A. de Heer, J. Phys. Chem. B **108**, 19912 (2004).

[4] L. X. Chen, W. H. Shan, C. X. Jiang, C. Chen, and H. M. Wang, Acta Phys. Sin. **68**, 168102 (2019).

[5] S. Das, D. Pandey, J. Thomas, and T. Roy, Adv. Mater. **31**, 1802722 (2019).

[6] D. Basu, M. J. Gilbert, L. F. Register, S. K. Banerjee, and A. H. MacDonald, Appl. Phys. Lett. **92**, 042114 (2008).

[7] C. G. Tao, L. Y. Jiao, O. V. Yazyev, Y. C. Chen, J. J. Feng, X. W. Zhang, R. B. Capaz, J. M. Tour, A. Zettl, S. G. Louie, H. J. Dai, and M. F. Crommie, Nat. Phys. **7**, 616 (2011).

[8] K. Wakabayashi, M. Fujita, H. Ajiki, and M. Sigrist, Phys. Rev. B **59**, 8271 (1999).

[9] L. Brey and H. A. Fertig, Phys. Rev. B **73**, 235411 (2006).

[10] K. Nakada, M. Fujita, G. Dresselhaus, and M. S. Dresselhaus, Phys. Rev. B **54**, 17954 (1996).

[11] S. Dutta, S. Lakshmi, and S. K. Pati, Phys. Rev. B **77**, 073412 (2008).

[12] H. Hsu and L. E. Reichl, Phys. Rev. B **76**, 045418 (2007).

[13] V. A. Saroka, M. V. Shuba, and M. E. Portnoi, Phys. Rev. B **95**, 155438 (2017).

[14] C. P. Chang, Y. C. Huang, C. L. Lu, J. H. Ho, T. S. Li, and M. F. Lin, Carbon **44**, 508 (2006).

[15] V. A. Saroka, K. G. Batrakov, V. A. Demin, and L. A. Chernozatonskii, J. Phys.: Condens. Matter **27**, 145305 (2015).

[16] L. Yang, M. L. Cohen, and S. G. Louie, Phys. Rev. Lett. **101**, 186401 (2008).

[17] Y. Lu, W. Lu, W. Liang, and H. Liu, Phys. Rev. B **88**, 165425 (2013).

[18] L. Yang, M. L. Cohen, and S. G. Louie, Nano Lett. **7**, 3112 (2007).

[19] B. S. Monozon and P. Schmelcher, Phys. Rev. B **99**, 165415 (2019).

[20] J. D. Cox and F. Javier Garcia de Abajo, Nat. Commun. **5**, 5725 (2014).

[21] J. D. Cox, R. Yu, and F. J. García de Abajo, Phys. Rev. B **96**, 045442 (2017).

[22] F. Karimi, A. H. Davoody, and I. Knezevic, Phys. Rev. B **97**, 245403 (2018).

[23] C. Attaccalite, E. Cannuccia, and M. Grüning, Phys. Rev. B **95**, 125403 (2017).

[24] Y. Wang and D. R. Andersen, J. Phys. D: Appl. Phys. **49**, 46LT01 (2016).

[25] Y. Wang and D. R. Andersen, J. Phys: Condens. Matter **28**, 475301 (2016).

[26] Y. Wang and D. R. Andersen, Phys. Rev. B **93**, 235430 (2016).

[27] C. Salazar, J. L. Cheng, and J. E. Sipe, Phys. Rev. B **93**, 075442 (2016).

[28] J. Wu, Y. Zheng, Z. Zeng, and R. Li, China Opt. Lett. **18**, 103201 (2020).

[29] F. Bonabi and T. G. Pedersen, Phys. Rev. B **99**, 045413 (2019).

[30] A. Bhatnagar, A. R. Chaudhuri, Y. H. Kim, D. Hesse, and M. Alexe, Nat. Commun. **4**, 2835 (2013).

[31] T. Rangel, B. M. Fregoso, B. S. Mendoza, T. Morimoto, J. E. Moore, and J. B. Neaton, Phys. Rev. Lett. **119**, 067402 (2017).

[32] S. Reich, J. Maultzsch, C. Thomsen, and P. Ordejón, Phys. Rev. B **66**, 035412 (2002).

[33] Y. Hancock, A. Uppstu, K. Saloriutta, A. Harju, and M. J. Puska, Phys. Rev. B **81**, 245402 (2010).

[34] R. B. Payod, D. Grassano, G. N. C. Santos, D. I. Levshov, O. Pulci, and V. A. Saroka, Nat. Commun. **11**, 82 (2020).

[35] J. Cayssol and J.-N. Fuchs, J. Phys.: Mater. **4**, 034007 (2021).

[36] J. E. Sipe and A. I. Shkrebtii, Phys. Rev. B **61**, 5337 (2000).

[37] To get the true edge states from numerical errors when they are nearly degenerate, an appropriate superposition of these two numerical eigenstates is performed to get the y components of the position operator in a form $r_{ssk}^{0;y} = 0$ for $s = \pm 1$ and nonzero $r_{(-1)(+1)k}^{0;y}$. Then the phases of the eigenstates for different bands s are chosen appropriately to give a real and smooth $r_{(\pm 1)sk}^{0;y}$.

[38] J. L. Cheng, N. Vermeulen, and J. E. Sipe, Phys. Rev. B **91**, 235320 (2015).

[39] F. Nastos and J. E. Sipe, Phys. Rev. B **74**, 035201 (2006).

[40] L. Chen, L. He, H. S. Wang, H. Wang, S. Tang, C. Cong, H. Xie, L. Li, H. Xia, T. Li *et al.*, Nat. Commun. **8**, 14703 (2017).

[41] G. Z. Magda, X. Jin, I. Hagymási, P. Vancsó, Z. Osváth, P. Nemes-Incze, C. Hwang, L. P. Biro, and L. Tapaszto, Nature (London) **514**, 608 (2014).